EPJ Photovoltaics **16**, 21 (2025)

https://doi.org/10.1051/epjpv/2025009

Available online at:
www.epj-pv.org

ORIGINAL ARTICLE OPEN ACCESS

On the annual energy yield of perovskite/silicon tandem modules with different bottom cell technologies and optimized top cell properties for different locations

Manvika Singh*, Jacopo Finazzo, Youri Blom, Mahesh Jayan, Carlos Ruiz Tobon, Arthur Weeber, Miroslav Zeman, Rudi Santbergen, and Olindo Isabella

Delft University of Technology, PVMD Group, Mekelweg 4, 2628 CD Delft, the Netherlands

Received: 21 October 2024 / Accepted: 24 February 2025

Abstract. At standard test conditions (STC), the performance of photovoltaic modules is compared using efficiency. As irradiance and module temperature fluctuate over the year and STC efficiency does not assess the performance of the module accurately in real world conditions, the annual energy yield is used instead as performance metric. Perovskite/silicon tandem solar cells are being massively researched and sought after in PV industry for their efficiency well above 34% with further growth perspective. In this work, to evaluate and compare performance of different perovskite/silicon tandem photovoltaic (PV) modules based on different bottom cell technologies, we use a hybrid modelling approach. Such approach, combining experimentally obtained and simulated current-voltage curves, flexibly predicts the annual energy yield of novel tandem PV modules via our PVMD toolbox and enables their optimization in any location. In particular, considering (i) mono- and bi-facial architectures, (ii) 2-terminal and 4-terminal module configurations, and (iii) silicon heterojunction or novel poly-SiO_x passivated c-Si solar bottom cells, we compare the annual energy yield of different perovskite/silicon tandem modules and we optimize their performance in different locations with respect to different perovskite thickness and bandgaps.

Keywords: Energy yield / perovskite/c-Si tandem / poly-SiO_x / 2T / 4T

1 Introduction

Crystalline silicon solar cells (c-Si) dominate the photovoltaic (PV) market. As single junction crystalline silicon (c-Si) solar cells are approaching their theoretical efficiency limit [1–3] with record conversion efficiency above 27% [4], perovskite/c-Si tandem solar cells are gaining attention [5–35]. Perovskite solar cells are being extensively studied in various domains, including simulation and optimization [36–43], fabrication [44–52], and energy yield analysis [53–65]. Perovskite/c–Si tandem solar cells have shown efficiencies of 34.6% [66] and have the potential to go beyond that. 2-terminal (2T) and 4-terminal (4T) configurations are typically considered for tandem solar cells and modules. In 2T configuration, the top and bottom cells are monolithically integrated and the current matching between them is crucial to obtain a high efficiency. In 4T configuration, the top and bottom cells are fabricated separately, and no current matching is required; but optical losses increase. This is due to additional charge transport layers required for top and bottom cells as well as the optical matching layer in between the component cells. More information about the 2T and 4T tandem configurations can be found in [6,67–69].

A performance metric more relevant than the efficiency, which is measured at standard test conditions (STC) [70], is the annual energy yield. This performance metric accounts for time-dependent and location-dependent variations in spectral irradiance and cell temperature, to which solar cells, and especially tandem devices, are sensitive. Dedicated software can be used to simulate from certain input data the irradiance-dependent and temperature-dependent current density-voltage (JV) curves and from those predict the energy yield of novel tandem device designs for various climate conditions [71,72], study their performance losses [73] or evaluate their degradation [74]. In this work, we introduce a hybrid experimental-modelling approach for predicting the energy yield of prospective tandem modules. We use measured IV curves of lab-scale c-Si solar cells based on carrier-selective passivating contacts (CSPCs), taken at different irradiance and temperature levels, and combine those with simulated IV curves of perovskite top cell endowed with different

* e-mail: msingh1@tudelft.nl

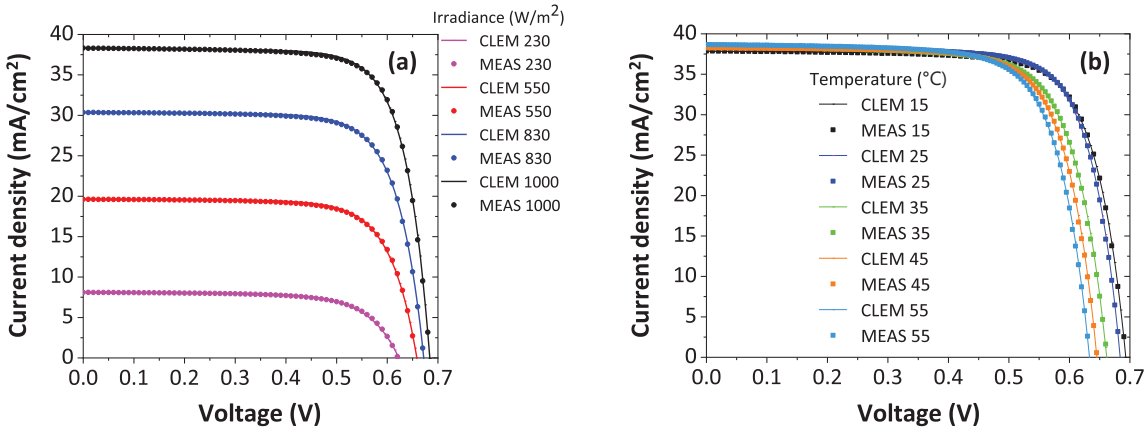

Fig. 1. Measured JV curves (denoted by Meas) and reconstructed JV curves by Calibrated Lumped Element Model (CLEM) of front side textured c-Si solar cell endowed with poly-SiO_x CSPCs (solar cell structure shown in Fig. 3b) for varying (a) irradiance for a fixed temperature of 25 °C and (b) temperature for a fixed irradiance of 1000 W/m^2.

absorber thickness and bandgap. Then, we combine such information in our PVMD toolbox [71] to predict the annual energy yield of perovskite/c-Si tandem modules with different bottom cell technologies and in different climatic conditions.

CSPCs passivate the silicon surface along with providing carrier selectivity. One way CSPCs are incorporated in c-Si solar cells is by depositing intrinsic and doped amorphous silicon layer on c-Si wafers as in silicon heterojunction (SHJ) solar cells [75–77]. Another way is by depositing thin tunnelling silicon di-oxide (SiO_2) on c-Si wafers followed by a doped polysilicon (poly-Si) layer as in Tunnel Oxide Passivated Contact (TOPCon) solar cells technology [78]. TOPCon technology has replaced the Passivated Emitter Rear Cell (PERC) and Al-based Back Surface Field (Al-BSF) technologies and is now actually dominating the PV market [79]. The world market share of TOPCon solar cells is anticipated to reach 60% in 2033 [79]. Poly-Si solar cells based on TOPCon technology have shown high efficiency [80–88], but poly-Si layers exhibit parasitic absorption losses [89]. To reduce the parasitic absorption in these layers, poly-SiO_x [90–96] and poly-SiC_x [97,98] are also being explored as CSPCs. Researchers have conducted studies on energy yield of perovskite/c-Si tandem solar cells with SHJ bottom solar cell. However not much attention has been devoted to the modelling of energy yield of perovskite/c-Si tandem solar cells with high temperature CSPCs bottom solar cells. In our previous work, we have shown the optical optimization and fabrication of perovskite/c-Si tandem solar cells where the bottom cell is endowed with novel poly-SiO_x-based CSPCs [94–96]. In this work, we extend that study to predict the annual energy yield of prospective perovskite/c-Si tandem modules with bottom poly-SiO_x CSPCs cells. To this end, (i) we use our physics-based comprehensive modelling framework in real world conditions; (ii) we optimize both the bandgap and thickness of the perovskite top absorber; and (iii) we evaluate, in reference to SHJ, the performance of poly-SiO_x bottom cell in 2T and 4T configurations for both mono- and bi-facial cell architectures.

2 Experimental

In this study, we use front/back contacted (FBC) poly-SiO_x based c-Si solar cell [96] to study the effect of high temperature CSPCs in tandem applications. JV measurements have been performed for different irradiance and temperature on FBC poly-SiO_x based c-Si solar cell using a AAA-class solar simulator which shines artificial light using xenon and halogen lamps with a spectrum close to standard air mass 1.5. The JV measurements at different temperatures are performed by cooling/heating the stage on which measurement sample is kept. Also, the JV measurements at different irradiance levels are performed by using polka dot beam splitters that scale down the intensity of the incident light without affecting the shape of the spectrum. JV curves at different irradiance and temperature of the FBC poly-SiO_x based c-Si solar cell are shown in Figures 1a and 1b, respectively. The irradiance ranges between 200 W/m^2 to 1000 W/m^2 and the temperature ranges from 15 °C to 55 °C. As expected, the J_{sc} increases with increasing illumination intensity and the V_{oc} decreases with increasing temperature. The fabrication details of FBC poly-SiO_x based c-Si solar cell are given elsewhere [96] and its schematic diagram is shown in Figure 3b.

3 Simulation approach

The PVMD toolbox has been used to calculate the energy yield of perovskite/c-Si tandem modules with different bottom cell technologies [71]. The PVMD toolbox consists of cell, module, weather, thermal and electrical models which together enable to simulate the energy yield of a solar cell or a PV module [71]. GenPro4 software is used to calculate the optical properties of the solar module [99]. We define the layer stack and give optical constants (refractive index and absorption coefficient) as well as the thickness of each layer as input in GenPro4. GenPro4 calculates the angle- and wavelength-resolved reflectance and absorptance of each layer in the module. The absorption

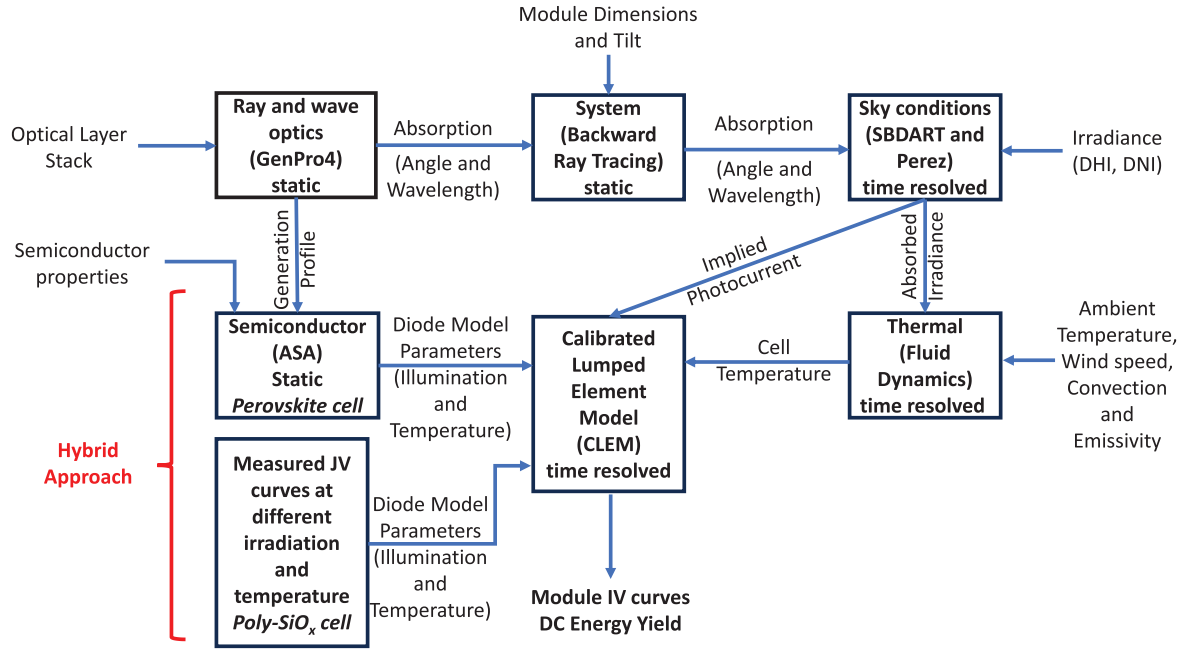

Fig. 2. Flowchart showing hybrid approach used to calculate the (annual) energy yield of tandem modules with poly-SiO_x bottom cell.

calculated in GenPro4 is also depth resolved. For the bi-facial tandem modules, such calculation is performed for both front and rear irradiance. The absorption in each layer is given as an input to the module part, which uses a ray tracing model [100] to calculate the absorption of the cells in the module. Note that the module comprises 60 series-connected and encapsulated cells. The angle- and wavelength-dependent absorption is given as an input to the weather model to calculate the photocurrent generated by each cell in the module. We use the Perez model to reconstruct the sky map from Diffused Horizontal Irradiance (DHI) and Direct Normal Irradiance (DNI). This sky map indicates the brightness of each part of the sky. The tilt and other mounting conditions are given as input in module part which calculates the sensitivity map. This sensitivity map is multiplied by the sky map to obtain the global tilted irradiance [101]. The sky map and therefore also the tilted irradiance are spectrally resolved. The spectral distribution is calculated by the SBDART model [102]. The thermal module then calculates the temperature of the cell, and the electrical part uses a calibrated lumped element model (CLEM) to compute the module JV curves and DC energy yield for every hour of the year. The implied photocurrent density (output of the weather module) and the other electrical parameters (extracted from simulated/measured JV) are given as input in the CLEM model to generate tandem JV curves. Note that this CLEM is based on a five-parameter single diode model in which each of the parameters are temperature and irradiance (corresponding photocurrent density) dependent. In our hybrid approach, the JV curves can either be obtained from measurements, or from semiconductor device simulations such as those carried out with ASA software [71,103,104]. For the perovskite/c-Si tandem device endowed with the reference SHJ bottom cell, the JV curves of both the top and the bottom cell are obtained from simulations. The schematic process flow of this simulation framework used to compute the energy yield of perovskite/c-Si tandem solar cells is shown in Figure 2. Our hybrid approach is an extension of the existing simulation framework [71] whereas the input JV parameters of the top perovskite solar cell have been simulated and the bottom poly-SiO_x c-Si solar cell has been experimentally measured.

4 Validation

The in-house developed and manufactured FBC poly-SiO_x solar cell [96], with a certified efficiency of 20.47%, has been used for validating the proposed modelling framework. The FBC poly-SiO_x solar cell has a front side texture and rear side flat interface. The refractive index (n), extinction coefficient (k) and thickness of n-type and p-type doped poly-SiO_x CSPCs have been taken from our earlier work [94]. Figure 3a shows the simulated absorptance and measured EQE of the FBC poly-SiO_x cell. The simulated values have an average deviation of 1.6% from the measured values, which shows that the simulated values are a good match with the measured values. The schematic of the simulated structure is shown in Figure 3b. Validation of EQE and JV of the reference 2T perovskite/c-Si tandem with SHJ bottom cell is shown in Figures 3c and 3d respectively.

Measured JV curves at varying irradiance and temperature of the FBC poly-SiO_x solar cell are given as dots in Figures 1a and 1b, respectively. This shows that, as expected, increasing irradiance increases the current and increasing temperature reduces voltage in these solar cells. These JV curves are used for parameter extraction which are given as an input to the electrical part of the PVMD

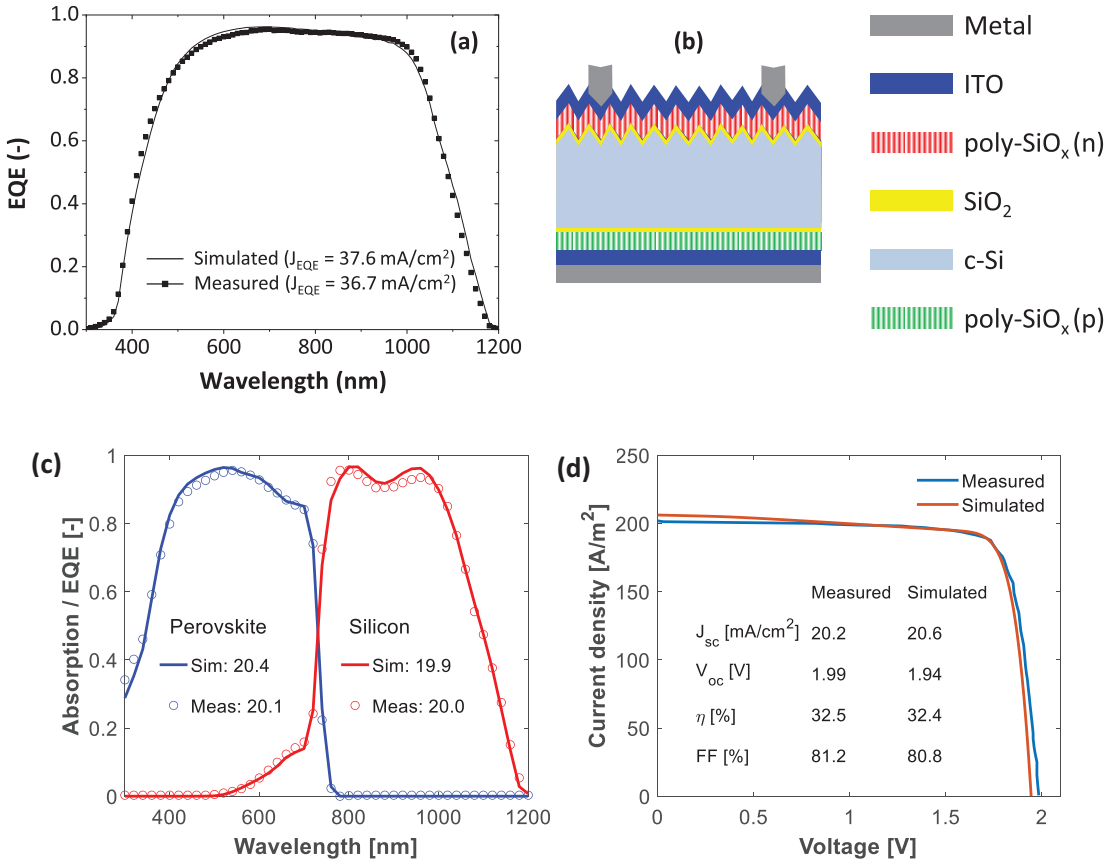

Fig. 3. (a) Comparison of simulated absorptance (black line) with EQE (black squares) for front back contacted (FBC) single side textured (SST) poly-SiO$_x$ passivated c-Si solar cell (b) solar cell structure used for simulation and measurement of EQE. Comparison of (c) simulated absorptance with EQE (given in [105]) and (d) simulated JV with measured JV (given in [105]) for the reference 2T perovskite/c-Si tandem with SHJ bottom cell.

toolbox. As explained in Section 3, the measured curves are fit using the five-parameter model, and the irradiance and temperature dependence of each of these five parameters is again parameterized. The average deviation between measured JV curves (details in Sect. 2) and reconstructed JV curves (from CLEM parameters) is less than 5%, showing that the fit is a good match. The JV curves of the top perovskite solar cell and the reference SHJ bottom cell [71,105] have been obtained by ASA simulations and their validation is shown in Figure 4. The main effect of increasing temperature is a decrease in the V_{oc}, which is clearly observed in both the JV-curves from measurement (of the poly-SiO$_x$ cell), and those from ASA simulation (of the perovskite and SHJ cells), and is included in our energy yield model. A secondary effect of increasing temperature, is a slight increase in J_{sc} due to bandgap variations. This is naturally included in the JV-curves obtained from measurement. However, this effect is not included in the JV-curves obtained from ASA simulations. This might lead to an underestimation of energy yield by a few percentage.

While the poly-SiO$_x$ solar cell is fabricated in-house and holds potential for improvement in both passivation quality and optical performance, the SHJ solar cell considered represents an optimized, high-efficiency device as described in reference [105]. In terms of parameters relevant to the energy yield model, transitioning from the SHJ to the poly-SiO$_x$-based solar cell results in a reduction in V_{oc}. This decline is primarily attributed to the poly-SiO$_x$ cell's lower passivation quality, which requires further optimization. Consequently this leads to an increase in recombination current density (J_o). Additionally, the SHJ solar cell demonstrates better carrier collection, as evident by a lower series resistance compared to the poly-SiO$_x$-based solar cell. Furthermore, differences in the optical constants of the carrier-selective passivation contacts (CSPCs) between the two c-Si technologies contribute to performance variations. The thicker poly-SiO$_x$ layer introduces higher parasitic absorption losses, slightly diminishing the optical performance of the poly-SiO$_x$ based solar cell compared to the SHJ solar cell.

5 Input parameters and structures

The FBC poly-SiO$_x$ c-Si solar cell, the 2T tandem based on mono-facial poly-SiO$_x$ cell, the 2T tandem based on bi-facial poly-SiO$_x$ cell, and the 4T tandem based on mono-facial poly-SiO$_x$ cell are shown in Figures 5a–5d, respectively. We have considered a front and rear side texturing in the bottom c-Si solar cell to achieve maximum

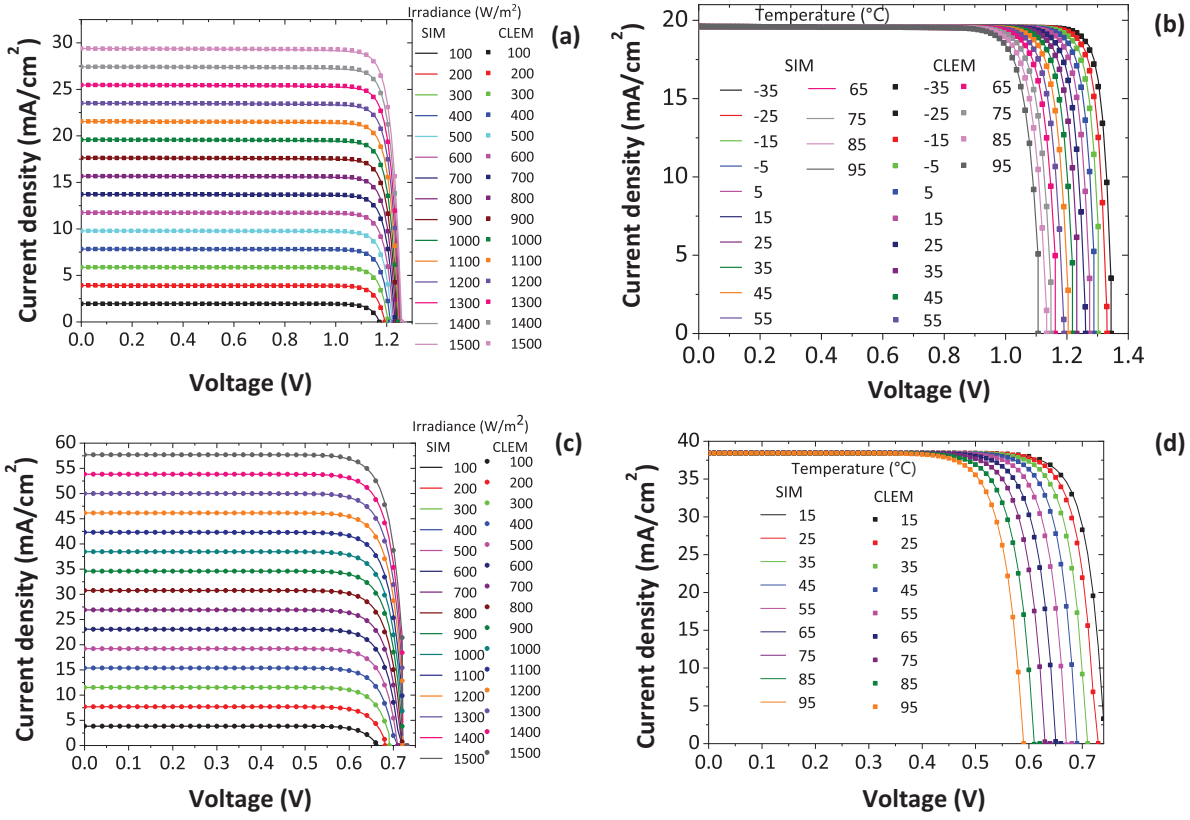

Fig. 4. Simulated JV curves in ASA and GenPro4 (denoted by SIM) and reconstructed JV curves by Calibrated Lumped Element Model (CLEM) of perovskite solar cell for varying (a) irradiance for a fixed temperature of 25 °C and (b) temperature for a fixed irradiance of 1000 W/m^2 and SHJ solar cell for (c) varying irradiance for a fixed temperature of 25 °C and (d) temperature for a fixed irradiance of 1000 W/m^2.

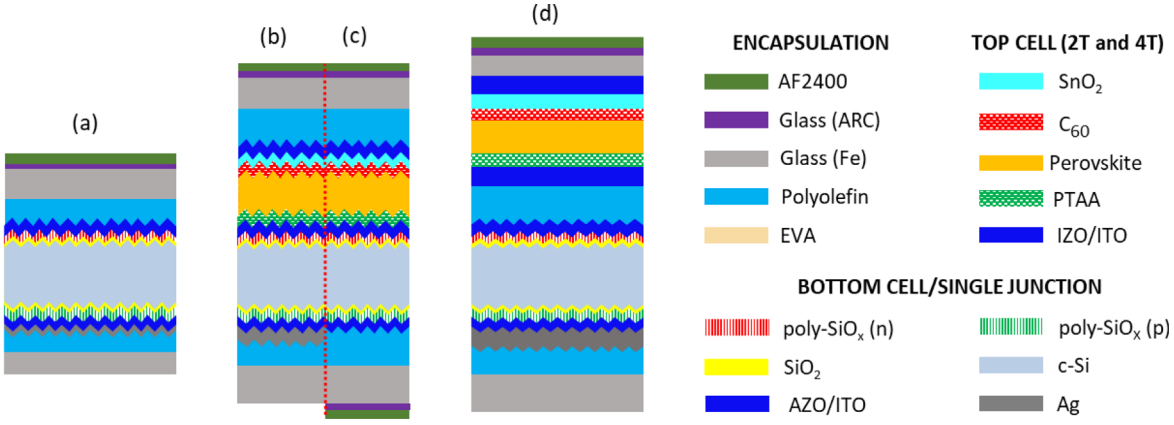

Fig. 5. Simulated solar modules archetypes: (a) single junction mono-facial encapsulated FBC poly-SiO_x solar cell, (b) 2T mono-facial encapsulated perovskite/c-Si tandem with poly-SiO_x bottom cell, (c) 2T bi-facial encapsulated perovskite/c-Si tandem with poly-SiO_x bottom cell, and (d) 4T mono-facial encapsulated perovskite/c-Si tandem with poly-SiO_x bottom cell. Flat/flat top cell is considered for 4T. In such configuration an ITO layer is added at rear of the top cell for hole collection. Glass (ARC) is used as an anti-reflection coating to reduce reflection losses whereas Glass (Fe) is the soda lime glass typically used as an encapsulant in PV modules [71].

absorption. Perovskite solar cell deposited on top of c-Si solar cell follows the same texturing in 2T. For the 4T tandem, a flat perovskite top cell is considered as the perovskite solar cell in this case is deposited on flat glass. The thickness of the various layers used in simulation is given in Table 1. Thickness of c-Si is chosen to be 160 µm to match with industrial standards.

Table 2 shows the various module parameters used in simulations. For bi-facial tandems (as shown in Fig. 5c), no rear metal is considered. Since, the rear TCO will increase the series resistance in bi-facial tandem, we consider twice the value of interconnection losses (ITO and metal resistance) in the bi-facial case. Cell to module losses such as the resistance losses due to additional top and bottom

Table 1. Input layer thickness of simulated solar cell structures.

2T and 4T tandem			
Perovskite top cell		c-Si bottom cell	
Layer	Thickness	Layer	Thickness
TOP ITO / IZO [2T,4T]	40 nm, 175 nm	Top ITO	75 nm
SnO_2	5 nm	poly-SiO_x (n type)	20 nm
C_{60}	7 nm	SiO_2	1.5 nm
Perovskite [2T,4T]	variable	c-Si bulk	160 µm
PTAA	23 nm	poly-SiO_x (p type)	30 nm
Bottom ITO [4T only]	175 nm	Bottom ITO	150 nm
		Ag	300 nm
	Encapsulation materials		
AF2400	93 nm	Glass-Fe10ppmM1	3000 µm
Glass ARC	53 nm	Polyolefin-UVT	450 µm

Table 2. Module and electrical parameters used in energy yield simulation.

Number of cell rows	10	Bypass diodes	3
Number of cell columns	6	Module thickness	0.5 cm
Cell length	15.675 cm	Module row spacing	800 cm
Cell width	15.675 cm	Module area	1.5749 m^2
Total number of cells	60	Edge spacing	1 cm
Cell spacing	0.3 cm	Module side spacing	2 cm
Metal and ITO resistance	0.0039 Ω [106]	Module azimuth	South-facing 0°, North-facing 180°
Metal coverage	2% [107,108]	Mounting height	50 cm

Table 3. Global Horizontal Irradiance (GHI), optimum tilt, latitude and longitude, average air mass (AM_{avg}) and average ambient temperature (T_{avg}) of different locations used in simulation. AM_{avg} and T_{avg} are averaged over the entire year.

Location	Annual global horizontal irradiance (GHI) (kWh/m^2)	Optimum tilt (°) [109]	Latitude and longitude	Average air mass (AM_{avg})	Average ambient temperature T_{avg} (°C)
Reykjavik (Iceland)	752	43	64.1470 °N 21.9408 °E	2.61	5.46
Rome (Italy)	1403	27	41.9028 °N 12.4964 °E	2.17	15.80
Alice Springs (Australia)	2203	−27	23.6980 °S 133.8807 °E	1.87	21.63

ITO, parasitic absorption losses due to encapsulation, spacing losses to account for the spacing between the cells and metal contact shading have been included. The location specific input parameters used in simulation, such as Global Horizontal Irradiance (GHI), optimum tilt, latitude and longitude, average Air Mass (AM) and average Ambient Temperature (T_{avg}) for each location are also included in Table 3. The architecture and input parameters of the double side textured reference SHJ tandem has been taken from [17,71,105].

6 Results and discussion

6.1 Energy yield at standard test conditions (STC)

Table 4 gives the parameters of SHJ and poly-SiO_x based c-Si solar cells and modules at STC. The 2T tandems have been current-matched for a perovskite bandgap of 1.68 eV. The matched photocurrent density of the 2T mono-facial tandem based on poly-SiO_x bottom cell is 19.5 mA/cm^2 for a 550-nm thick perovskite absorber. Using the hybrid

Table 4. Cell and module parameters for c-Si solar cell modules based on silicon heterojunction (SHJ) (reference) and poly-SiO_x technologies. Parameters for both single junction (SJ) and tandem structures are given below. Thickness of c-Si is fixed to 160 µm, while the perovskite thickness has been adjusted to obtain photocurrent density (J_{ph}) matching at STC. For 2T, $J_{ph,top} = J_{ph,bottom}$, while the bandgap of perovskite is 1.68 eV.

Cell type	Perovskite thickness [nm]	Silicon thickness [µm]	Photo-current density $J_{ph,top}$, $J_{ph,bottom}$ (mA/cm^2)	Rear side photo-current density (mA/cm^2)	STC power [W_p]	STC module efficiency [%]
SHJ SJ	n.a.	160	37.8	–	323	20.5
Poly-SiO_x SJ	n.a.	160	37.4	–	260	16.5
2T SHJ Tandem	700	160	19.9	35.7	455	28.9
2T Poly-SiO_x Tandem	550	160	19.5	34.8	421	26.7
4T SHJ Tandem	700	160	18.4, 17.7	–	416	26.4
4T Poly-SiO_x Tandem	700	160	18.4, 17.4	–	382	24.3

Table 5. Temperature coefficients (TCs) of SHJ and poly-SiO_x based c-Si modules as well as perovskite based modules. These temperature coefficients have been calculated from simulated and measured JV curves of c-Si solar cells based on SHJ and poly-SiO_x technology as well as perovskite solar cells respectively.

Cell type	TC $_{Voc}$ (%/K)	TC_{Jsc} (%/K)	TC_{Pmpp} (%/K)
SHJ SJ	–0.264	–0.001	–0.322
Poly-SiO_x SJ	–0.233	0.039	–0.25
Perovskite SJ	–0.143	0.0009	–0.174

modelling approach, we can predict various parameters of the module comprising 2T mono-facial tandem devices based on poly-SiO_x bottom cells, such as the power (421 W_p) and the module efficiency (26.7%) at STC conditions. In the case of 4T mono-facial configuration, a thicker perovskite of 700 nm is used for simulations as there are no current matching restrictions and a thicker perovskite is expected to give better performance. The module comprising 4T mono-facial tandem devices based on poly-SiO_x bottom cell delivers STC power output of 382 W and a module efficiency of 24.3%. We note the STC power output of the 2T tandem is 10.3% higher than that of the 4T tandem. The 4T tandem output is lower due to additional optical losses caused by the intermediate optical matching layers [110] and electrical losses due to the additional ITO layer at the rear of the perovskite top cell. SHJ tandem solar cells present higher output power to poly-SiO_x tandem solar cells. This is due to the lower passivation quality and larger parasitic absorption losses of doped poly-SiO_x CSPCs and ITO in the tandem based on poly-SiO_x bottom cell. Unlike the SHJ tandem, wherein the tunnel recombination junction (TRJ) is optimized for highest performance [17,71,105], the ITO layer considered in the poly-SiO_x tandem has been taken from the fabricated poly-SiO_x based single junction (SJ) solar cell [96] and has not been optimized for the tandem case. The TRJ of the tandem device based on poly-SiO_x bottom cell could be further optimized to increase the annual energy yield, but it is not the focus of this work. Table 5 shows the calculated voltage, current and power temperature coefficients (TCs) for SHJ and poly-SiO_x single junction (SJ) solar modules as well as perovskite SJ solar modules. For poly-SiO_x c-Si solar cell, the TC are calculated from measured JV curves as given in Figures 1a and 1b. For SHJ and perovskite solar cell, the TCs are calculated from simulated JV curves obtained from ASA [71,105] as shown in Figure 4. We find the TCs of the SHJ cell are more negative as compared to poly-SiO_x solar cell. The more negative temperature coefficients observed in SHJ cells could be due to a higher sensitivity of V_{oc} to temperature in SHJ solar cells as their passivation layers are deposited at lower temperatures. In contrast, poly-SiO_x-based cells, where passivation layers are deposited at higher temperature, have better thermal stability and experience less temperature-dependent reduction in $V_{oc.}$This indicates that the poly-SiO_x based solar cells might be more temperature stable as compared to SHJ solar cells. In this work we use the TCs of bottom cell of tandem to explain the differences in the performance of tandem as the top perovskite solar cell is similar in both cases.

6.2 Energy yield in outdoor conditions

In this section, the energy yield of novel 2T and 4T mono-facial tandem modules based on poly-SiO_x bottom cell is optimized with respect to different perovskite thicknesses and bandgaps. The bi-facial case is also considered for the 2T tandem module. Location chosen for this part of the study is Rome (see Tab. 3). The input parameters and structure of the tandem devices are given in Section 5. On the other hand, tandem devices based on SHJ bottom cell have already been optimized in earlier studies [71,111–114].

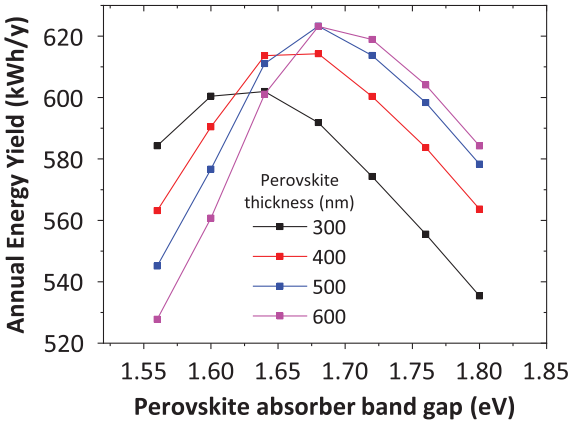

Fig. 6. Annual energy yield of 2T mono-facial tandem module based on poly-SiO_x bottom cell as function of top cell perovskite absorber bandgap and thickness. Shift in optimum bandgap is seen for increasing thickness of perovskite. The simulations have been carried out in Rome as location at an optimum tilt of 27°.

6.2.1 2T mono-facial tandem module based on poly-SiO_x bottom cell

As we see from Table 4, a 550-nm thick perovskite absorber is required to reach photocurrent density matching in 2T tandem device with poly-SiO_x bottom cell. In outdoor conditions, one has to evaluate the opto-electric performance of the tandem as function of perovskite bandgap and thickness, which affect both V_{oc} and J_{sc}. Hence, we have optimized the bandgap and thickness of the perovskite absorber layer to maximize the annual energy yield of the 2T tandem device in Rome at an optimum tilt of 27°. Figure 6 shows such optimization wherein annual energy yield of the 2T perovskite/poly-SiO_x tandem module is simulated for a range of perovskite bandgaps (from 1.56 eV to 1.80 eV) and for different perovskite absorber thicknesses (from 300 to 600 nm). From Figure 6, we find the optimum perovskite bandgap for 300-nm thick perovskite absorber is 1.64 eV, which gives 602 kWh/y in terms of annual energy yield. This optimum value increases to 1.68 eV for a 600-nm thick perovskite absorber thickness, which gives 623 kWh/y. Since the optimum energy yield is obtained around photocurrent density matched condition, we find that by increasing the perovskite bandgap in 2T perovskite/c-Si tandem cell, the optimum energy yield is obtained for a thicker perovskite absorber.

6.2.2 2T vs 4T mono-facial tandem module based on poly-SiO_x bottom cell

In this section, the simulation results related to 2T and 4T tandem devices both based on poly-SiO_x solar cell are compared, again as function of perovskite absorber thickness and bandgap. The input structure and parameters for the 4T tandem module have been also given in Section 5. Figure 7a shows annual energy yield for varying perovskite absorber thickness (from 300 to 900 nm) of both 2T and 4T tandem modules based on poly-SiO_x bottom cell. Note that the perovskite bandgap has been fixed to 1.68 eV for these simulations. We observe an increase in the annual energy yield of the 2T tandem module (592 kWh/y to 624 kWh/y) as the perovskite thickness increases from 300 nm to 550 nm. As the perovskite thickness is further increased beyond 550 nm, the annual energy yield gradually decreases. The annual energy yield for 900-nm thick perovskite thickness is 615 kWh. This shows that at 550 nm, top and bottom sub-cells are current matched and, so, the highest annual energy yield is obtained. In general, we observe the perovskite absorber is limiting the tandem's total current for thinner perovskite absorbers whereas the c-Si bulk is limiting the current for thicker perovskite absorbers. From our previous work, we have seen similar trends for total photocurrent of 2T tandem device [95]. On the other hand, for the 4T tandem module based on poly-SiO_x bottom cell, the current matching is not required. The annual energy yield for 4T tandem increases for increasing perovskite thickness (545 kWh at 300 nm to 569 kWh at 700 nm). On increasing the perovskite thickness after 700 nm, a slight decrease in energy yield is seen (567 kWh at 900 nm). Hence, 700 nm is the optimal perovskite thickness for 4T tandem configuration. The annual energy yield of the optimized 2T and 4T tandems modules are 624 kWh/y and 569 kWh/y, respectively. The annual energy yield of the 2T tandem module is higher than the annual energy yield of the 4T tandem module by an average 8.5%. This value is reduced from the 10.3% mark at STC (see Tab. 4) due to varying real world spectral conditions. A lower annual energy yield in 4T tandem module can be attributed to the additional optical and electrical losses in the 4T configuration as compared to the 2T one due to additional charge transport layers in top and bottom cells of 4T tandem.

Figure 7b shows again the annual energy yield of 2T and 4T tandem modules based on poly-SiO_x bottom cell but for varying perovskite bandgaps (from 1.60 to 1.90 eV) and fixed thickness of the perovskite absorber (550 nm and 700 nm for 2T and 4T configurations, respectively). These values are chosen since they realize the highest annual energy yield (see Fig. 7a). In Figure 7b we observe that the 2T tandem module based on poly-SiO_x bottom cell is more sensitive than the 4T counterpart to the perovskite absorber bandgap. This is due to the current mismatch conditions that affect the 2T tandem configuration. For the perovskite absorber exhibiting bandgaps lower than 1.68 eV, the c-Si bottom cell is limiting and for perovskite bandgaps above 1.68 eV, the top perovskite cell is limiting. So, in the 2T configuration, the optimum bandgap for 550-nm thick perovskite is 1.68 eV. By increasing the perovskite bandgap from 1.60 eV to 1.68 eV, the annual energy yield increases from 567 kWh/y to 624 kWh/y. Above the 1.68 eV bandgap value, the annual energy yield decreases. However, for the 4T configuration, varying the perovskite bandgap from 1.60 eV to 1.68 eV, the annual energy yield increases from 562 kWh/y to only 569 kWh/y. Optimal perovskite bandgap in this case is achieved at 1.81 eV at which the yield is 572 kWh/y. On further increasing the perovskite bandgap, the energy yield decreases to 560 kWh/y at perovskite bandgap of 1.9 eV. On varying the perovskite bandgap, the energy yield of 4T tandem varies by only 1.78% unlike the 2T case where the energy yield varies by around 10%.

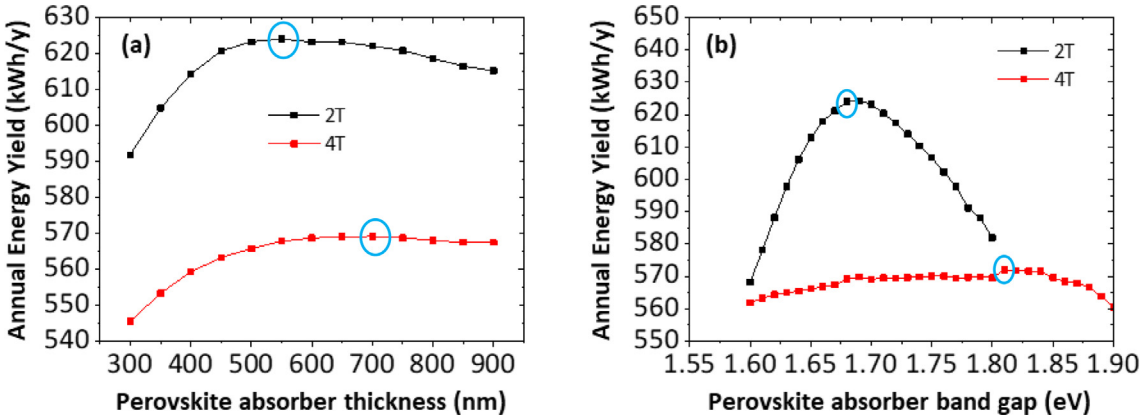

Fig. 7. Annual energy yield of 2T and 4T perovskite/poly-SiO_x tandem for (a) varying perovskite thickness (perovskite bandgap is fixed to 1.68 eV for 2T and 4T tandem) and (b) varying perovskite bandgap (perovskite thickness is fixed to 550 nm for 2T and 700 nm for 4T). The 4T and 2T poly-SiO_x simulations have been carried out at Rome at an optimum tilt of 27°. The blue circles indicate the optimal perovskite thickness and bandgap respectively.

6.2.3 2T mono-facial vs bi-facial tandem module based on poly-SiO_x bottom cell

Bi-facial modules can benefit from the additional irradiation on the rear side of the module. However, in the 2T configuration, this also poses an additional challenge while pursuing the current matching condition as the rear-side irradiance is fully absorbed by the bottom cell. In this section, annual energy yield of 2T bi-facial perovskite/c-Si tandem modules are simulated with respect to the spectral albedo of several materials, such as dry grass, green grass, white paint and snow. Note an in-house developed ray-tracing model [100,101,115] is used to calculate both front and rear side spectrally resolved irradiance for every hour of the year. The wavelength dependent reflectance or spectral albedo of dry grass, green grass, white paint and snow are shown in Figure 8a. The average reflectance over the wavelength range from 300 nm to 1200 nm is highest for snow (94.3%) followed by white paint (65.1%), green grass (36.5%) and dry grass (25.3%). Snow is close to an ideal reflector and is also considered in this study. Here, we have considered our standard current-matched case of 2T tandem module based on poly-SiO_x bottom cell with 550-nm thick perovskite absorber with 1.68 eV bandgap. Again, the modelling location is Rome for a tilt of 27°. In order for the results to be comparable, for a mono-facial tandem module the ground reflected irradiance has also been taken into account. Spectral albedo of dry grass has been chosen for these simulations.

First, for surfaces with different spectral albedo, the thickness of the perovskite absorber is varied while keeping fixed the bandgap to 1.68 eV. These results are shown in Figure 8b. As expected, the annual energy yield of the 2T bi-facial tandem module increases on surfaces with higher spectral albedo as the sunlight reflected from the ground is absorbed in c-Si absorber and adds to its current. As expected, the highest annual energy yield is seen for the 2T bi-facial tandem module on snow. For perovskite thicknesses greater than 550 nm, the increased current density from the bottom cell starts limiting the performance. So the annual energy yield can be increased for thicker perovskite absorber. With respect to the 2T mono-facial configuration, the 2T bi-facial configuration on snow shows an increase in annual energy yield of 2.5% (4.5% and 5.3%) for 300-nm (600-nm and 900-nm) thick perovskite absorber. It is evident that a thicker perovskite is needed to current match the extra current generated due to rear absorption in bi-facial case. We observe in Figure 8b, in case of snow, that the optimum perovskite thickness increases from 550 nm of the mono-facial configuration to 700 nm of the bi-facial configuration. In the former case, the maximum annual energy yield is 624 kWh/y while in the latter the annual energy yield is 652 kWh/y.

In Figure 8c, the perovskite bandgap is varied between 1.56 eV and 1.80 eV while the thickness is set to 550 nm. For perovskite bandgaps below 1.68 eV, the c-Si current is limiting and the additional light absorption from the rear side of the tandem module increases the module's current and, consequently, its annual energy yield as compared to the 2T mono-facial configuration. Hence, the increase in annual energy yield for 2T bi-facial tandem modules with respect to 2T mono-facial tandem modules is higher for perovskite bandgaps lower than 1.68 eV. With respect to the 2T mono-facial tandem module poly-SiO_x tandem and in case of snow, the 2T bi-facial tandem module shows an increase of 7.5% (4% and 1.9%) for 1.56 eV (1.68 eV and 1.80 eV) perovskite bandgap. We remind the optimum perovskite bandgap and thickness for the 2T mono-facial tandem module being 1.68 eV and 550 nm, respectively. As the spectral albedo increases, we see a slight shift towards lower perovskite bandgaps. To conclude, the optimum perovskite bandgap on snow is 1.67 eV and, for perovskite thickness of 550 nm, the resulting maximum annual energy yield is 650 kWh/y.

Notably, the bi-facial configuration demonstrates flexibility in design, with a broader range of perovskite bandgaps (1.65–1.68 eV) and thicknesses (500–800 nm) resulting in energy yield variations of less than 1%. This indicates the robustness of the bi-facial design to parameter variations. In general, for all surfaces, a perovskite bandgap

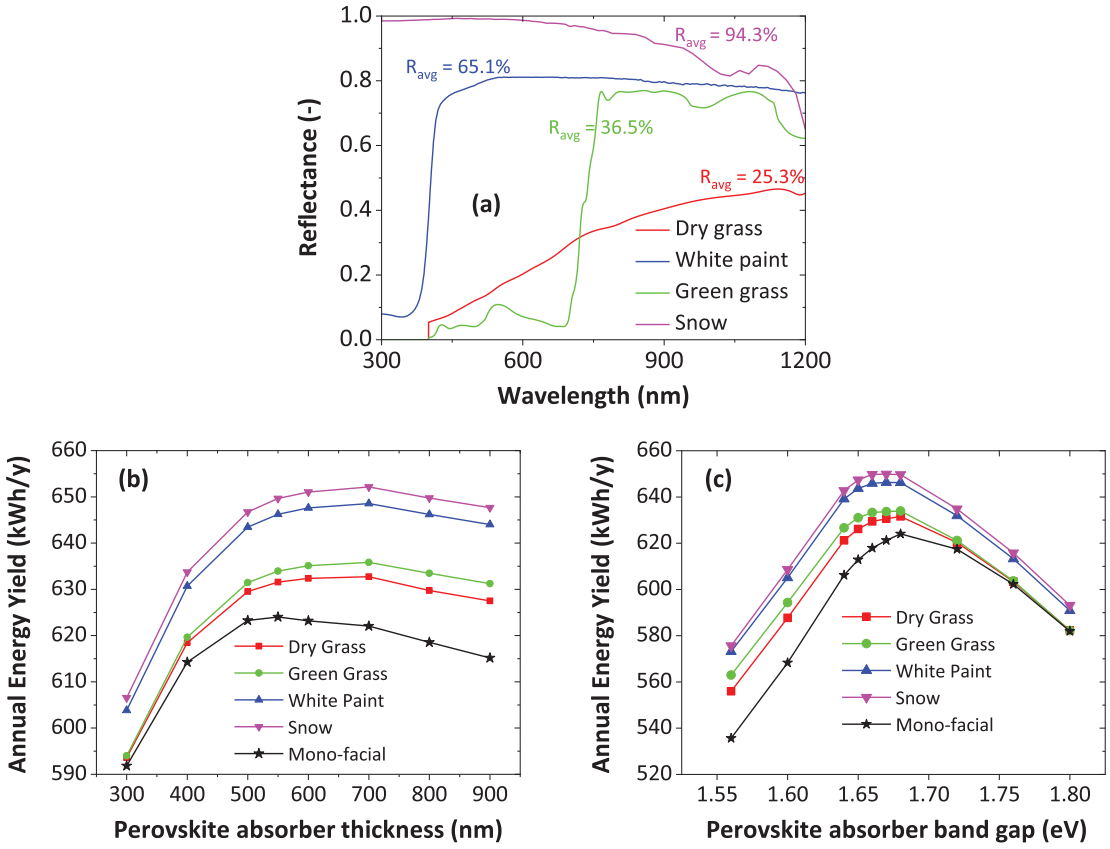

Fig. 8. (a) Wavelength-dependent reflectance for different surfaces; Annual Energy Yield of 2T bi-facial tandem based on poly-SiO_x bottom cell for (b) varying top cell perovskite thickness on different ground surfaces (perovskite bandgap = 1.68 eV) and (c) varying top cell perovskite bandgap on different ground surfaces (perovskite thickness = 550 nm). The above simulations are carried out in Rome at a tilt of 27°.

of 1.68 eV and a thickness of 700 nm yield the best performance for a 2T bi-facial perovskite/c-Si tandem module with a poly-SiO_x bottom cell. In comparison, for the 2T mono-facial configuration, the optimal perovskite bandgap and thickness are 1.68 eV and 550 nm, respectively.

When fabricating mono-facial and bi-facial modules together, it is feasible to use a common perovskite bandgap of 1.68 eV and a thickness of 550 nm, ensuring efficient performance across both configurations. This approach highlights the potential for standardizing key parameters, simplifying the fabrication process, and maintaining high performance under diverse outdoor conditions.

6.3 Comparison of SJ and tandem modules based on poly-SiO_x and SHJ bottom cells

In this section, the annual energy yield of tandem modules with different bottom cell technologies, namely SHJ and poly-SiO_x CSPCs, has been simulated for different locations using the PVMD toolbox. Tilting the photovoltaic module at optimum angle increases the incident irradiance on the plane of the array. The optimum tilt for testing cities, Reykjavik (Iceland), Rome (Italy) and Alice Springs (Australia), are given in Table 3. The motivation for choosing these cities is that they cover a wide range of latitudes and an increasing annual global horizontal irradiance (GHI), as shown in Table 3. The single junction and tandem module archetypes have been shown in the Figure 5, while detailed input parameters are given in Section 5.

6.3.1 SJ and 2T tandem modules

Figures 9a, 9b and 9c show the modelled annual energy yield and specific energy yield of SJ and 2T tandem modules based on SHJ (reference) or poly-SiO_x technologies in Reykjavik, Rome and Alice Springs, respectively. Optimized perovskite thickness of 700 nm and 550 nm are used for simulating 2T tandem modules based on SHJ or poly-SiO_x bottom cells, respectively (see Figs. 7a, 7b and Tab. 4). Results of SJ SHJ and poly-SiO_x modules are also analysed.

At STC, we observe the output power of 2T tandem modules based on SHJ (poly-SiO_x) bottom cells is higher than the SJ SHJ (poly-SiO_x) module by ~41% (~62%) (see Tab. 4). Also in outdoor conditions, the 2T modules outperform SJ modules and, with increasing irradiance at different testing cities, the annual energy yield of the various module technologies increases. The annual energy yield of 2T tandem modules based on poly-SiO_x bottom cells is 377 kWh/y, 624 kWh/y and 931 kWh/y in Reykjavik, Rome and Alice Springs, respectively.

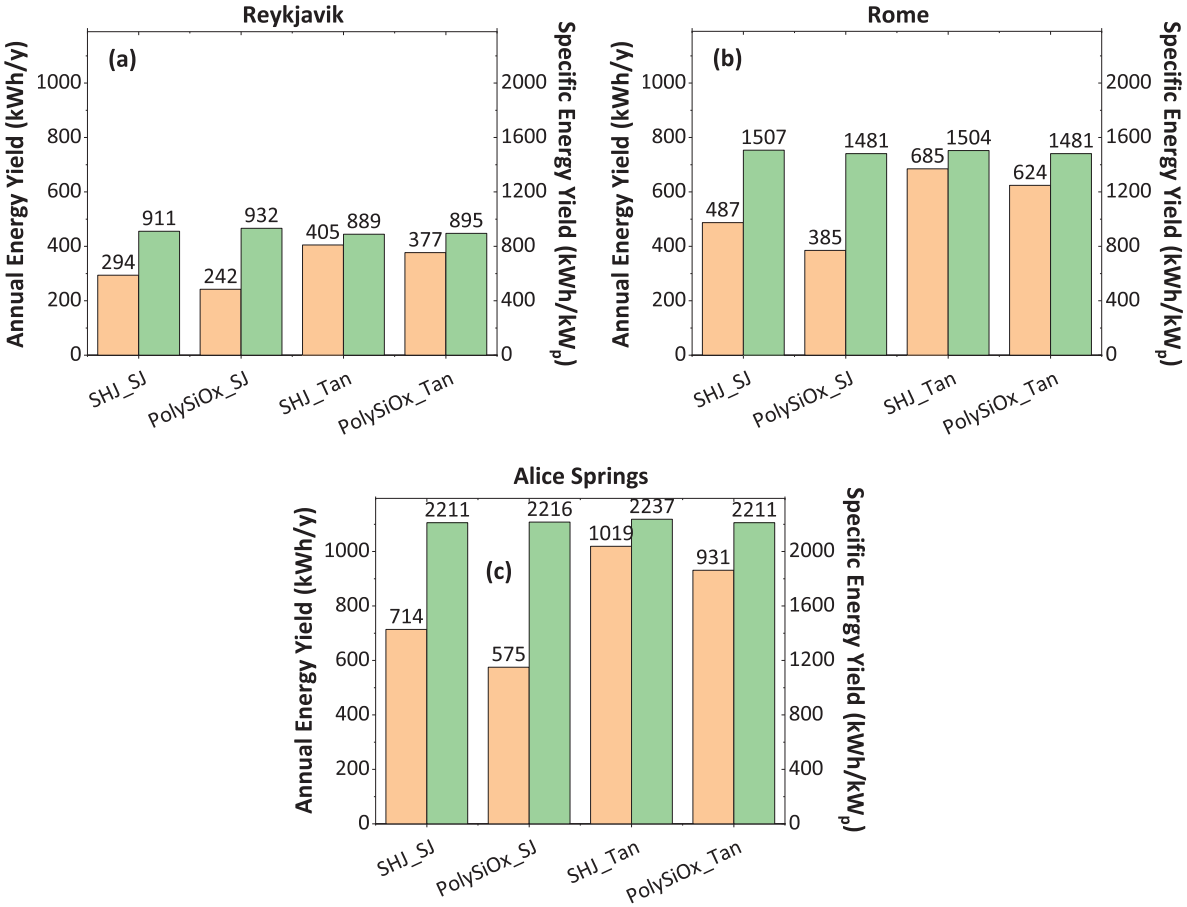

Fig. 9. Annual energy yield (left axis, orange bars) and specific energy yield (right axis, green bars) of single junction silicon heterojunction (SHJ_SJ) cells module, single junction poly-SiO_x (Poly-SiO_x_SJ) cells module, 2T tandem module based on SHJ bottom cell (SHJ_Tan) and 2T tandem module based on poly-SiO_x bottom cell (PolySiO_x_Tan) in (a) Reykjavik, (b) Rome and (c) Alice Springs.

In contrast, SJ modules based on poly-SiO_x cells realize an annual energy yield of 242 kWh/y, 385 kWh/y and 575 kWh/y in Reykjavik, Rome and Alice Springs, respectively. Therefore, from SJ to 2T tandem modules based on poly-SiO_x, a gain in annual energy yield of 56%, 62% and 62% can be expected in Reykjavik, Rome and Alice Springs respectively. The slightly lower tandem gain for Reykjavik can be attributed to the incident spectrum in Reykjavik being farthest from the STC spectrum (AM1.5) as compared to Rome and Alice Springs for which the tandem was current matched (See AM_{avg} in Tab. 3).

Figures 9a, 9b and 9c show that the annual energy yield of 2T tandem modules based on SHJ bottom cells is higher than that of the 2T tandem module based on poly-SiO_x bottom cells. The specific energy yield, defined as the annual energy yield over the STC power and simply indicated with kWh/kW_p, is an important parameter to compare the performance of different cell technologies relative to their STC performance. The specific energy yield of the 2T tandem module based on poly-SiO_x bottom cells is only ∼1.5% (∼1.2%) lower than that of the reference 2T tandem module based on SHJ bottom cells tandem in Rome (Alice Springs). Conversely, for locations with lower irradiance such as Reykjavik, the specific energy yield of the 2T tandem module based on poly-SiO_x bottom cells is 0.7% higher than that of the 2T tandem module based on SHJ bottom cells. We explain this results as follows. At lower irradiance, the voltage and the power output are more sensitive to temperature change [116]. Hence, the 2T tandem module based on SHJ bottom cells suffers from higher power loses in case of temperature changes as compared to the poly-SiO_x-based counterpart due to the more negative temperature coefficient of SHJ bottom cells (see Tab. 5).

6.3.2 4T tandems modules

The series connection of 4T tandem is simulated by simulating the top and bottom cell JV curves separately for every hour of the year. The resistance values of the ITO layers for both top and bottom cell curves are included. Finally, the top and bottom cell's power is added to obtain the total DC power (energy yield) of the 4T tandem. Here we assume to top cells are not connected to the bottom cells, so top and bottom operate independently (each have their on MPPT). Figures 10a, 10b and 10c show the annual

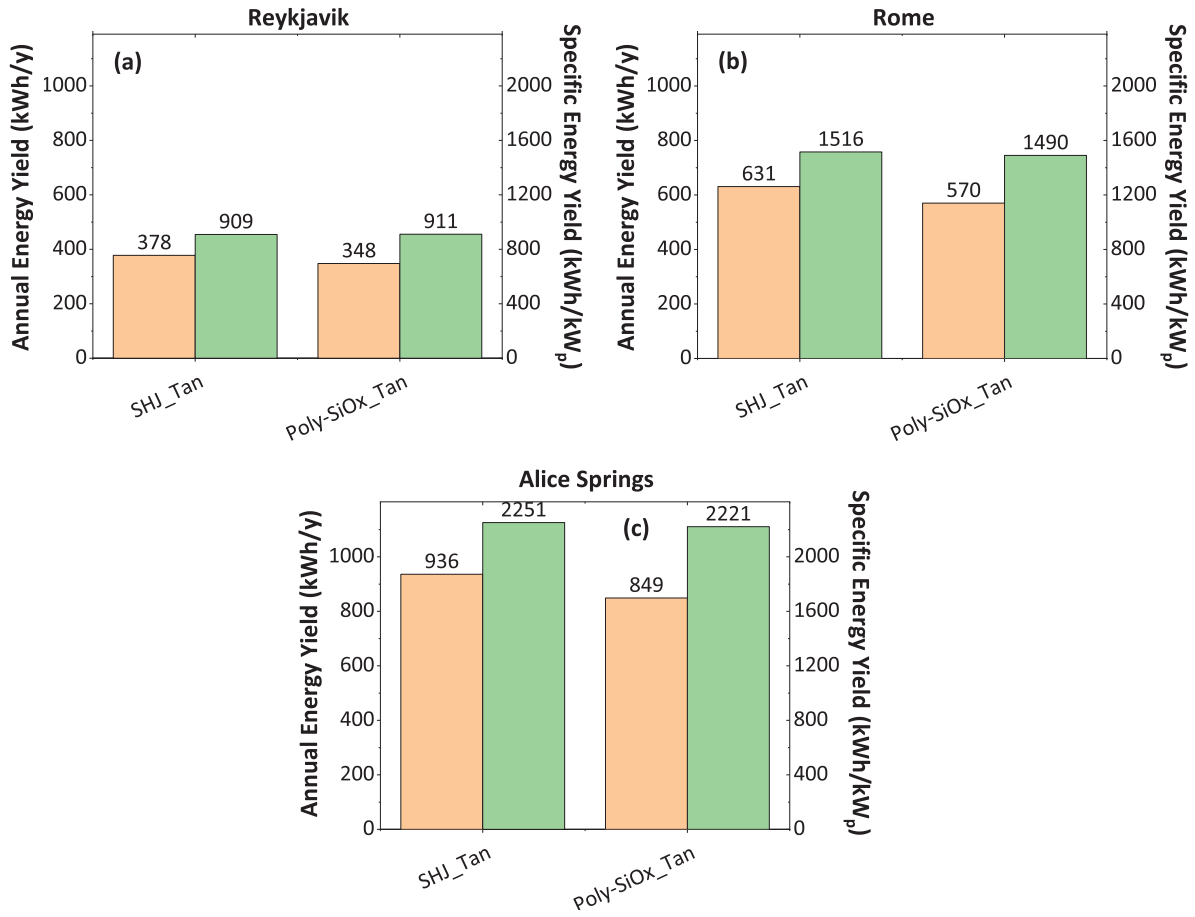

Fig. 10. Annual energy yield (orange bars) and specific energy yield (green bars) of 4T tandem modules based on SHJ and poly-SiO_x bottom cells in (a) Reykjavik, (b) Rome and (c) Alice Springs. Optimized tilt, given in Table 3, are used in the simulations. The perovskite is absorber is 700-nm thick and its bandgap is 1.68 eV.

energy yield and the specific energy yield of 4T tandem modules based on SHJ or poly-SiO_x bottom cells in Reykjavik, Rome and Alice Springs, respectively. In these simulations, the perovskite absorber is 700-nm thick and its bandgap is fixed at 1.68 eV (see Fig. 7a as well as Tab. 4). Although the optimal perovskite bandgap for the 4T configuration is 1.81 eV, we chose a 1.68 eV bandgap for 4T tandem simulations as it closely aligns with the optimal of 2T configuration. Additionally, the differences in energy yield between the two bandgaps are minimal in 4T case (see Fig. 7b). The annual energy yield of the 4T tandem based on poly-SiO_x bottom cells is 348 kWh/y, 570 kWh/y and 849 kWh/y in Reykjavik, Rome and Alice Springs, respectively. In contrast, the annual energy yield of the 4T tandem module based on SHJ bottom cells is higher that of the 4T module based on poly-SiO_x bottom cells by 8.7%, 10.8% and 10.4% in Reykyavik, Rome and Alice Springs, respectively. This is due to the additional opto-electrical losses experienced by the 4T tandem module based on poly-SiO_x bottom cells compared to its SHJ-based counterpart, similarly to the loss in performance at STC (See Tab. 4). The specific energy yield of 4T tandem modules based on poly-SiO_x bottom cells decreases with respect to that of the SHJ-based counterpart by 1.7% (1.3%) in Rome (Alice Springs). However, similarly to the 2T tandem modules' results, the specific energy yield of the 4T tandem module based on poly-SiO_x bottom cells is 0.2% higher than that of the SHJ-based counterpart in Reykjavik.

6.3.3 2T bi-facial and mono-facial tandem modules

Figures 11a, 11b and 11c show the comparison between 2T bi-facial tandem modules based on SHJ or poly-SiO_x bottom cells for different spectral albedos in Reykjavik, Rome and Alice Springs, respectively. For these bi-facial simulations, we have used the perovskite thickness that gives the current matched condition in 2T mono-facial case, i.e. 700 nm for SHJ-based tandem module and 550 nm for poly-SiO_x-based tandem (see Tab. 4). Also, the optimized perovskite bandgap of 1.68 eV is used in this simulation. The highest annual energy yield values are obtained on snow, which has the largest average spectral albedo of 94.3% (see Fig. 8a). The annual energy yield of 2T bi-facial tandem modules based on SHJ (poly-SiO_x) bottom cells is 420 kWh/y (397 kWh/y) in Reykjavik, 699 kWh/y (650 kWh/y) in Rome and 1033 kWh/y (964 kWh/y) in Alice Springs. As in the mono-facial configuration case, the difference in annual energy yield between SHJ-based and

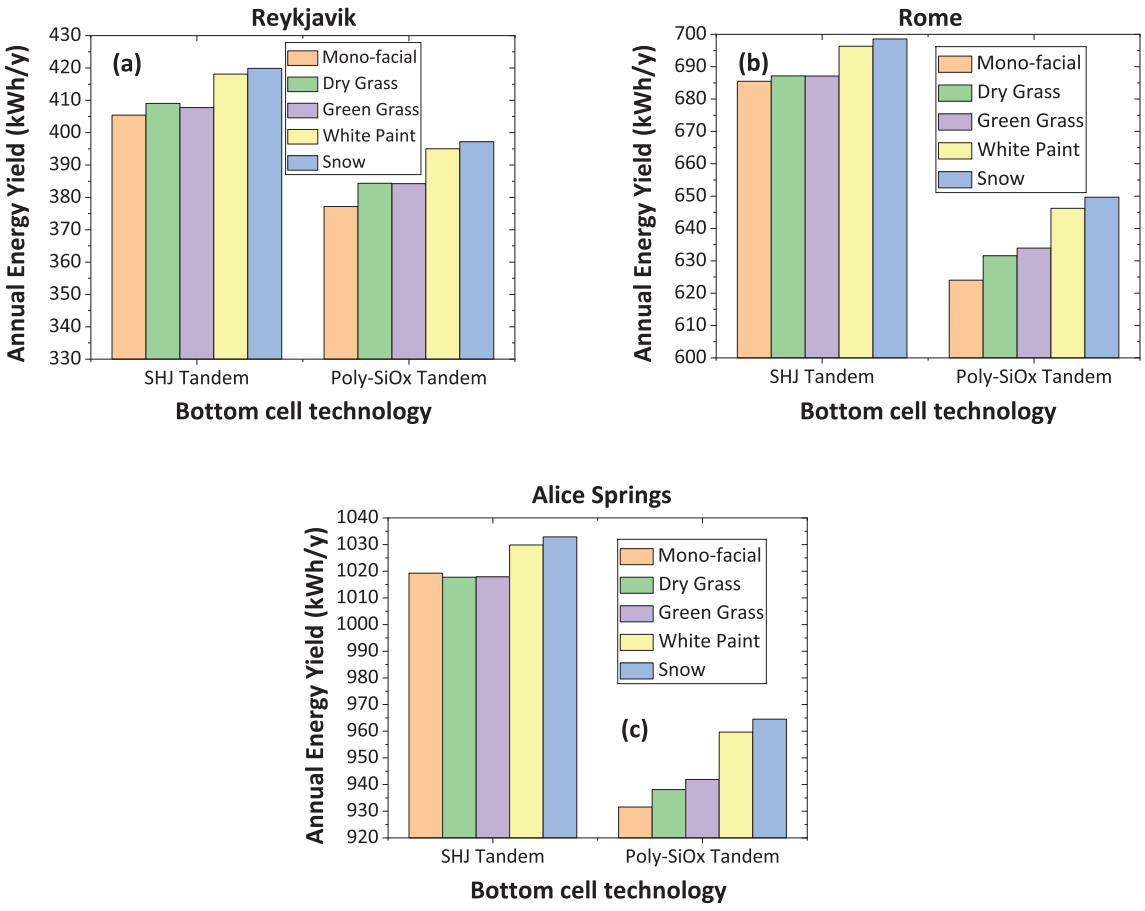

Fig. 11. Annual energy yield of 2T bi-facial tandem modules based on SHJ or poly-SiO_x bottom cells in (a) Reykjavik, (b) Rome and (c) Alice Springs for different reflecting materials (dry grass, green grass, white paint and snow). Results are compared with mono-facial configuration. The perovskite absorber thickness is set to 700 nm (550 nm) for SHJ-based (poly-SiO_x-based) tandem module. Its bandgap is 1.68 eV. Optimized tilt is considered for each location (Tab. 3).

poly-SiO_x-based tandem modules is higher in places like Rome (+7.5%) and Alice Springs (+7%) and lower in Reykjavik (+5.7%) due to the voltage of the SHJ-based tandem module being more sensitive to change in temperature in places with lower irradiance like Reykjavik.

From Figures 11a, 11b and 11c, we observe that the relative annual energy yield difference between the 2T tandem modules based on SHJ bottom cells with respect to the poly-SiO_x-based counterpart decreases with increasing spectral albedo in all testing cities. For example, in Rome, the annual energy yield of the 2T mono-facial tandem based on SHJ bottom cells is higher than that of the poly-SiO_x-based counterpart by 9.8% but decreases to 7.5% in bi-facial configuration for the case of snow. Since the photocurrent density generated from the rear-side irradiance of the SHJ solar cell is higher than that of the poly-SiO_x-based c-Si solar cell in the 2T configuration (see Tab. 4), the reduced difference in energy yield between the SHJ and poly-SiO_x-based cells in the bi-facial case (compared to the mono-facial case) cannot be attributed to optical factors. To explain this, the average operating temperature (T_{avg}), open circuit voltage ($V_{oc\text{-}avg}$), and short circuit current ($I_{sc\text{-}avg}$) of the 2T tandem modules based on SHJ or poly-SiO_x bottom cells in Rome are given in Table 6. The increased irradiance in bi-facial tandem modules increases both the photogenerated current and the voltage. However, the latter increase is curbed by the increase in operating cell temperature due to the increase in absorbed irradiance in the bi-facial tandem modules (see Tab. 6) [117]. Due to the more negative temperature coefficient of the SJ SHJ module (see Tab. 5), the $V_{oc\text{-}avg}$ is slightly lower in the 2T tandem modules based on SHJ bottom cells than in the poly-SiO_x-based counterparts. Hence, the voltage gain from mono-facial to bi-facial configuration is smaller in 2T tandem modules based on SHJ bottom cells than in the poly-SiO_x-based counterparts (see Tab. 6). Similarly, the increase in operating temperature due to the additional photogenerated current in bi-facial configuration increases the current more in the 2T tandem module based on poly-SiO_x bottom cells than in the SHJ-based counterpart due to the more positive current temperature coefficient of the SJ poly-SiO_x module (see Tab. 5). Hence, the difference between the 2T bi-facial tandem module based on SHJ bottom cells and the 2T bi-facial tandem module based on poly-SiO_x bottom cells decreases with increasing spectral albedo.

Table 6. Average output parameters of 2T tandem modules based on SHJ or poly-SiO_x bottom cells in Rome.

Modules output parameters	SHJ technology			Poly-SiO_x technology		
	2T mono-facial tandem	2T bi-facial tandem on snow	Absolute increase	2T mono-facial tandem	2T bi-facial tandem on snow	Absolute increase
Average operating temperature T_{avg} (°C)	18.35	18.53	0.18	18.51	18.73	0.22
Average output voltage $V_{oc\text{-}avg}$ (V)	55.19	55.54	0.35	53.43	53.93	0.5
Average output current $I_{SC\text{-}avg}$ (A)	1.66	1.7	0.04	1.62	1.67	0.05

7 Conclusions

In this work, we have used a hybrid approach (combination of simulation and experimental data) in an advanced simulation framework to calculate the annual energy yield and the specific energy yield of novel 2T and 4T tandem modules based on poly-SiO_x bottom cells. This approach makes our device simulations flexible and is especially useful for predicting annual energy yield of tandem modules with novel materials or architectures.

Our results reveal several critical insights into the performance of poly-SiO_x-based tandem modules. Under standard test conditions (STC), we calculated power outputs of 421 Wp and 382 Wp for 2T mono-facial and 4T tandem modules, respectively, based on poly-SiO_x bottom cells. In outdoor realistic conditions, the optimized annual energy yield of a 2T mono-facial and 4T tandem modules based on poly-SiO_x bottom cells is 624 kWh/y and 572 kWh/y, respectively, in the testing city of Rome. By leveraging bifacial configurations, we further enhanced the annual energy yield of 2T tandem modules to 652 kWh/y on reflective surfaces such as snow, showcasing the potential of poly-SiO_x-based tandems in high-albedo environments.

Using our simulation framework, we have determined the optimum perovskite thickness and bandgap for various tandem configurations. For the mono-facial 2T tandem, the optimal parameters are a bandgap of 1.68 eV and a thickness of 550 nm, while for the 4T perovskite/c-Si tandem, they are 1.81 eV and 700 nm. However, a common perovskite bandgap of 1.68 eV can be effectively utilized for both 2T and 4T configurations, as the 4T tandem demonstrates less than 2% variation in energy yield within the 1.68–1.81 eV bandgap range. In the 2T bi-facial configuration, a bandgap of 1.68 eV and a thickness of 700 nm generally perform best across all surface types. However, we observe that a broader range of perovskite bandgaps (1.65–1.68 eV) and thicknesses (500–800 nm) results in energy yield variations of less than 1% in the bi-facial case. This highlights the flexibility of our modeling framework, which allows for the optimization of a common set of parameters across different conditions.

In this study, we have experimentally shown that the poly-SiO_x passivated c-Si solar cell can be more thermally stable as compared to the modelled SHJ solar cell presented in our previous study [71]. For locations with lower irradiance such as Reykjavik, the specific energy yield of 2T (4T) tandem module based on poly-SiO_x bottom cells is 0.7% (0.2%) higher than that of SHJ-based counterpart due to the effects of poly-SiO_x solar cells' temperature coefficient on tandem being more significant at lower irradiance. Using bi-facial tandem modules on snow, the annual energy yield difference between 2T tandem modules based on SHJ and poly-SiO_x bottom cells can be reduced. The increased rear irradiance in bi-facial configuration increases its operating temperature leading to lesser gain in performance of 2T bi-facial tandem based on SHJ bottom cells as compared to the poly-SiO_x-based counterpart due to the difference in their temperature coefficients.

Acknowledgments

The authors thankfully acknowledge NWO JSP III (680-91-011) program for financial support.

Funding

This research was funded by NOW JSP III grant number (680-91-011).

Conflicts of interest

The authors have nothing to disclose.

Data availability statement

This article has no associated data generated and/or analyzed.

Author contribution statement

Conceptualization, M. Singh; Methodology, M. Singh; Software, M. Singh, Y. Blom and C.R. Tobon; Validation, M. Singh; Formal Analysis, M. Singh; Investigation, M. Singh, J. Finazzo and M. Jayan; Resources, M. Singh; Data Curation, M. Singh; Writing – Original Draft Preparation, M. Singh; Writing – Review & Editing, O. Isabella and R. Santbergen; Visualization, M. Singh; Supervision, O. Isabella and R. Santbergen; Project Administration, O. Isabella; Funding Acquisition, O. Isabella, M. Zeman and A. Weeber.

References

1. W. Shockley, H.J. Quiesser, Detailed balance limit of efficiency of p-n junction solar cells, J. Appl. Phys. **32**, 510 (1961)
2. L.C. Andreani, A. Bozzola, P. Kowalczewsk et al., Silicon solar cells: toward the efficiency limits, Adv. Phys. X **4**, 1548305 (2019)
3. R. Armin, H. Martin, W.G. Stefan et al., Reassessment of the limiting efficiency for crystalline silicon solar cells, IEEE J. Photovolt. **3**, 1184 (2013)
4. LONGi Sets a New World Record of 27.09% for the Efficiency of Silicon Heterojunction Back-Contact (HBC) Solar Cells (2023). https://www.longi.com/en/news/heterojunction-back-contact-battery/
5. K.A. Bush, A.F. Palmstrom, J.Y. Zhengshan et al., 23.6%-efficient monolithic perovskite/silicon tandem solar cells with improved stability, Nat. Energy **2**, 1 (2017)
6. N.N. Lal, Y. Dkhissi, W. Li et al., Perovskite tandem solar cells, Adv. Energy Mater. **7**, 1602761 (2017)
7. F. Sahli, J. Werner, B.A. Kamino et al., Fully textured monolithic perovskite/silicon tandem solar cells with 25.2% power conversion efficiency, Nat. Mater. **17**, 820 (2018)
8. Oxford PV perovskite solar cell achieves 28% efficiency, Press Release by Oxford PV (2018). https://www.pv-magazine.com/2018/12/20/tandems-at-28/
9. G. Nogay, F. Sahli, J. Werner et al., 25.1\%-efficient monolithic perovskite/silicon tandem solar cell based on a p-type monocrystalline textured silicon wafer and high-temperature passivating contacts, ACS Energy Lett. **4**, 844 (2019)
10. J. Zheng, H. Mehrvarz, C. Liao et al., Large-area 23\%-efficient monolithic perovskite/homojunction-silicon tandem solar cell with enhanced UV stability using down-shifting material, ACS Energy Lett. **4**, 2623 (2019)
11. E. Kohnen, M. Jost, A.B. Morales-Vilches et al., Highly efficient monolithic perovskite silicon tandem solar cells: analyzing the influence of current mismatch on device performance, Sustain. Energy Fuels **3**, 1995 (2019)
12. R. Schmager, M. Langenhorst, J. Lehr et al., Methodology of energy yield modelling of perovskite-based multi-junction photovoltaics, Opt. Express **27**, A507 (2019)
13. Y. Liu, Y. Li, Y. Wu et al., High-efficiency silicon heterojunction solar cells: materials, devices and applications, Mater. Sci. Eng. R: Rep. **142**, 100579 (2020)
14. S. Gharibzadeh, I.M. Hossain, P. Fassl et al., 2D/3D Heterostructure for semitransparent perovskite solar cells with engineered bandgap enables efficiencies exceeding 25% in four-terminal tandems with silicon and CIGS, Adv. Funct. Mater. **30**, 1909919 (2020)
15. F. Gota, M. Langenhorst, R. Schmager et al., Energy yield advantages of three-terminal perovskite-silicon tandem photovoltaics, Joule **4**, 2387 (2020)
16. Oxford PV hits new world record for solar cell, Press Releases by Oxford PV (2020). https://www.oxfordpv.com/news/oxford-pv-hits-new-world-record-solar-cell
17. A. Al-Ashouri, E. Kohnen, B. Li et al., Monolithic perovskite/silicon tandem solar cell with >29\% efficiency by enhanced hole extraction, Science **370**, 1300 (2020)
18. A. Rohatgi, K. Zhu, J. Tong et al., 26.7% efficient 4-terminal perovskite-silicon tandem solar cell composed of a high-performance semitransparent perovskite cell and a doped poly-Si/SiOx passivating contact silicon cell, IEEE J. Photovolt. **10**, 417 (2020)
19. H.H. Park, J. Kim, G. Kim et al., Transparent electrodes consisting of a surface-treated buffer layer based on tungsten oxide for semitransparent perovskite solar cells and four-terminal tandem applications, Small Methods **4**, 2000074 (2020)
20. A.S. Subbiah, F.H. Isikgor, C.T. Howells et al., High-performance perovskite single-junction and textured perovskite/silicon tandem solar cells via slot-die-coating, ACS Energy Lett. **5**, 3034 (2020)
21. J. Xu, C.C. Boyd, J.Y. Zhengshan et al., Triple-halide wide–band gap perovskites with suppressed phase segregation for efficient tandems, Science **367**, 1097 (2020)
22. B. Chen, S.W. Baek, Y. Hou et al., Enhanced optical path and electron diffusion length enable high-efficiency perovskite tandems, Nat. Commun. **11**, 1257 (2020)
23. Z. Wang, X. Zhu, S. Zuo et al., 27%-efficiency four-terminal perovskite/silicon tandem solar cells by sandwiched gold nanomesh, Adv. Funct. Mater. **30**, 1908298 (2020)
24. P.S.C. Schulze, A.J. Bett, M. Bivour et al., 25.1\% high-efficient monolithic perovskite silicon tandem solar cell with a high band gap perovskite absorber, Sol. RRL **4**, 2000152 (2020)
25. World Record: Efficiency of perovskite silicon tandem solar cell jumps to 29.15 per cent, Press release by HZB (2020). https://www.helmholtz-berlin.de/pubbin/news_seite?nid=21020;sprache=en
26. World record again at HZB: Almost 30% efficiency for next-generation tandem solar cells, Press Releases by HZB (2021). https://www.helmholtz-berlin.de/pubbin/news_seite?nid=23248;sprache=en;seitenid=1
27. J. Liu, E. Aydin, J. Yin et al., 28.2%-efficient, outdoor-stable perovskite/silicon tandem solar cell, Joule **5**, 3169 (2021)
28. 2 New world records: perovskite-on-silicon-tandem solar cells, Press Releases by CSEM, EPFL (2022). https://csem.cdn.prismic.io/csem/f46abbd1-6fe4-4554-9e0e-053152b390aa_CP2022-EPFL-worldrecord-EN.pdf
29. Y. Wu, P. Zheng, J. Peng et al., 27.6% perovskite/c-Si tandem solar cells using industrial fabricated TOPCon device, Adv. Energy Mater. **12**, 2200821 (2022)
30. S. Mariotti, K. Jager, M. Diederich et al., Monolithic perovskite/silicon tandem solar cells fabricated using industrial p-type polycrystalline silicon on oxide/passivated emitter and rear cell silicon bottom cell technology, Solar RRL **6**, 2101066 (2022)
31. Z. Ying, Z. Yang, J. Zheng et al., Monolthic perovskite/black-silicon tandems based on tunnel oxide passivated contacts, Joule **6**, 2644 (2022)
32. Y. Yao, P. Hang, B. Li et al., Phase-stable wide-bandgap perovskites for four-terminal perovskite/silicon tandem solar cells with over 30% efficiency, Small **18**, 2203319 (2022)
33. World record back at HZB: Tandem solar cell achieves 32.5 percent efficiency, Press Release by HZB (2022). https://www.helmholtz-berlin.de/pubbin/news_seite?nid=24348;sprache=en

34. KAUST claims 33.7% efficiency for perovskite/silicon tandem solar cell, PV magazine (2023). https://www.pv-magazine.com/2023/05/30/kaust-claims-33-7-efficiency-for-perovskite-silicon-tandem-solar-cell/
35. LONGi sets a new world record of 33.9% for the efficiency of crystalline silicon-perovskite tandem solar cells (2023). https://www.longi.com/en/news/new-world-record-for-the-efficiency-of-crystalline-silicon-perovskite-tandem-solar-cells/
36. A.J. Riquelme, K. Valadez-Villalobos, P.P. Boix et al., Understanding equivalent circuits in perovskite solar cells. Insights from drift-diffusion simulation, Phys. Chem. Chem. Phys. **24**, 15657 (2022)
37. T. Moot, J.B. Patel, G. McAndrews et al., Temperature coefficients of perovskite photovoltaics for energy yield calculations, ACS Energy Lett. **6**, 2038 (2021)
38. F. Azri, A. Meftah, N. Sengouga et al., Electron and hole transport layers optimization by numerical simulation of a perovskite solar cell, Sol. Energy **181**, 372 (2019)
39. L. Lin, L. Jiang, P. Li et al., Simulated development and optimized performance of CsPbI3-based all-inorganic perovskite solar cells, Sol. Energy **198**, 454 (2020)
40. V. Sebastian, J. Kurian et al., Simulation and optimization studies on CsPbI3-based inorganic perovskite solar cells, Sol. Energy **221**, 99 (2021)
41. H. Abedini-Ahangarkola, S. Soleimani-Amiri, S.G. Rudi, Modeling and numerical simulation of high-efficiency perovskite solar cell with three active layers, Sol. Energy **236**, 724 (2022)
42. N.K. Sinha, D.S. Ghosh, A. Khare et al., A comprehensive guide to bifacial perovskite solar cells: simulation and optimization, Adv. Theory Simul. **7**, 2300633 (2024)
43. R. Ghosh, A. Singh, P. Agarwal et al., Study on effect of different HTL and ETL materials on the perovskite solar cell performance with TCAD simulator, Mater. Today: Proc. (2023)
44. J.Y. Kim, J.-W. Lee, H.S. Jung et al., High-efficiency perovskite solar cells, Chem. Rev. **120**, 7867 (2020)
45. F.H. Isikgor, S. Zhumagali, L.V.T. Merino et al., Molecular engineering of contact interfaces for high-performance perovskite solar cells, Nat. Rev. Mater. **8**, 89 (2023)
46. Z. Zhang, L. Qiao, K. Meng et al., Rationalization of passivation strategies toward high-performance perovskite solar cells, Chem. Soc. Rev. **52**, 163 (2023)
47. F. Qin, J. Chen, J. Liu et al., Design of high-efficiency perovskite solar cells based on inorganic and organic undoped double hole layer, Sol. Energy **262**, 111796 (2023)
48. A.D. Taylor, Q. Sun, K.P. Goetz et al., A general approach to high-efficiency perovskite solar cells by any antisolvent, Nat. Commun. **12**, 1878 (2021)
49. G. Li, Z. Su, L. Canil et al., Highly efficient pin perovskite solar cells that endure temperature variations, Science **379**, 399 (2023)
50. D.-K. Lee, N.-G. Park et al., Materials and methods for high-efficiency perovskite solar modules, Solar RRL **6**, 2100455 (2022)
51. S. Liu, V.P. Biju, Y. Qi et al., Recent progress in the development of high-efficiency inverted perovskite solar cells, NPG Asia Mater. **15**, 27 (2023)
52. Y. Yu, F. Zhang, T. Hou et al., A review on gas-quenching technique for efficient perovskite solar cells, Solar RRL **5**, 2100386 (2021)
53. M.T. Hörantner, H.J. Snaith, Predicting and optimising the energy yield of perovskite-on-silicon tandem solar cells under real world conditions, Energy Environ. Sci. **10**, 1983 (2017)
54. M. Lehr, M. Langenhorst, R. Schmager et al., Energy yield modelling of perovskite/silicon two-terminal tandem PV modules with flat and textured interfaces, Sustain. Energy Fuels **2**, 2754 (2018)
55. M. Jošt, E. Köhnen, A.B. Morales-Vilches et al., Textured interfaces in monolithic perovskite/silicon tandem solar cells: advanced light management for improved efficiency and energy yield, Energy Environ. Sci. **11**, 3511 (2018)
56. G. Coletti, S.L. Luxembourg, L.J. Geerligs et al., Bifacial four-terminal perovskite/silicon tandem solar cells and modules, ACS Energy Lett. **5**, 1676 (2020)
57. S. Orooji, U.W. Paetzold, Energy yield modeling of Perovskite-Silicon tandem photovoltaics: degradation and total lifetime energy yield, Energy Technol. **12**, 2400998 (2024)
58. M. De Bastiani, A.J. Mirabelli, Y. Hou et al., Efficient bifacial monolithic perovskite/silicon tandem solar cells via bandgap engineering, Nat. Energy **6**, 167 (2021)
59. F. Gota, M. Langenhorst, R. Schmager et al., Energy yield advantages of three-terminal perovskite-silicon tandem photovoltaics, Joule **4**, 2387 (2020)
60. B. Lipovšek, M. Jošt, Š. Tomšic et al., Energy yield of perovskite solar cells: influence of location, orientation, and external light management, Sol. Energy Mater. Sol. Cells **234**, 111421 (2022)
61. P. Lopez-Varo, M. Amara, S. Cacovich et al., Dynamic temperature effects in perovskite solar cells and energy yield, Sustain. Energy Fuels **5**, 5523 (2021)
62. M. Remec, Š. Tomšic, M. Khenkin et al., From sunrise to sunset: unraveling metastability in perovskite solar cells by coupled outdoor testing and energy yield modelling, Adv. Energy Mater. **2024**, 2304452 (2024)
63. Š. Tomšic, M. Jošt, K. Brecl et al., Energy yield modeling for optimization and analysis of perovskite-silicon tandem solar cells under realistic outdoor conditions, Adv. Theory Simul. **6**, 2200931 (2023)
64. M. Jošt, B. Lipovšek, B. Glažar et al., Perovskite solar cells go outdoors: field testing and temperature effects on energy yield, Adv. Energy Mater. **10**, 2000454 (2020)
65. R.H. Ahangharnejhad, W. Becker, J. Jones et al., Environmental impact per energy yield for bifacial perovskite solar cells outperforms crystalline silicon solar cells, Cell Rep. Phys. Sci. **1**, 100216 (2020)
66. 34.6%! Record-breaker LONGi Once Again Sets a New World Efficiency for Silicon-perovskite Tandem Solar Cells (2024). https://www.longi.com/en/news/2024-snec-silicon-perovskite-tandem-solar-cells-new-world-efficiency/
67. Y. Ko, H.J. Park, C. Lee et al., Recent progress in interconnection layers for hybrid photovoltaic tandems, Adv. Mat. **32**, 2002196 (2020)
68. H. Li, W. Zhang, Perovskite tandem solar cells: from fundamentals to commercial deployment, Chem. Rev. **120**, 9835 (2020)
69. M. Jost, L. Kegelmann, L. Korte et al., Monolithic perovskite tandem solar cells: a review of the present status and advanced characterization methods toward 30% efficiency, Adv. Mat. **10**, 1904102 (2020)
70. A.H.M. Smets et al., *Solar Energy: The physics and engineering of photovoltaic conversion, technologies and systems* (UIT Cambridge, 2016), Chapter 5

71. M. Vogt, C.R. Tobon, A. Alcaniz et al., Introducing a comprehensive physics-based modelling framework for tandem and other PV systems, Sol. Energy Mater. Sol. Cells **247**, 111944 (2022)
72. Š. Tomšic, M. Jošt, K. Brecl, M. Topic, B. Lipovšek, Energy yield modeling for optimization and analysis of perovskite-silicon tandem solar cells under realistic outdoor conditions, Adv. Theory Simul. **6**, 2200931 (2023)
73. Y. Blom, M.R. Vogt, C.M.R. Tobon, R. Santbergen, M. Zeman, O. Isabella, Energy loss analysis of two-terminal tandem PV systems under realistic operating conditions-revealing the importance of fill factor gains, Sol. RRL **7**, 2200579 (2023)
74. S. Orooji, U.W. Paetzold, Energy yield modeling of perovskite–silicon tandem photovoltaics: degradation and total lifetime energy yield, Energy Technol. **12**, 2400998 (2024)
75. M. Taguchi, A. Terakawa, E. Maruyama, M. Tanaka, Obtaining a higher Voc in HIT cell, Prog. Photovolt. Res. Appl. **13**, 481 (2005)
76. M. Taguchi, A. Yano, S. Tohoda et al., 24.7% record efficiency HIT solar cell on thin silicon wafer, IEEE J. Photovolt. **4**, 96 (2013)
77. K. Masuko, M. Shigematsu, T. Hashiguchi et al., Achievement of more than 25% conversion efficiency with crystalline silicon heterojunction solar cell, IEEE J. Photovolt. **4**, 1433 (2014)
78. F. Feldmann, M. Bivour, C. Reichel et al., Passivated rear contacts for high-efficiency n-type Si solar cells providing high interface passivation quality and excellent transport characteristics, Sol. Energy Mater. Sol. Cells **120**, 270 (2014)
79. VDMA, V.D.M.u.A, International Technology Roadmap for Photovoltaic, fourteenth ed. (2023)
80. A. Richter, J. Benick, F. Feldmann et al., n-Type Si solar cells with passivating electron contact: Identifying sources for efficiency limitations by wafer thickness and resistivity variation, Sol. Energy Mater. Sol. Cells **173**, 96 (2017)
81. G. Yang, A. Ingenito, O. Isabella et al., IBC c-Si solar cells based on ion-implanted poly-silicon passivating contacts, Sol. Energy Mater. Sol. Cells **158**, 84 (2016)
82. F. Haase, C. Hollemann, S. Schafer et al., Laser contact openings for local poly-Si-metal contacts enabling 26.1\ %-efficient POLO-IBC solar cells, Sol. Energy Mater. Sol. Cells **186**, 184 (2018)
83. F. Feldmann, C. Reichel, R. Muller et al., The application of poly-Si/SiOx contacts as passivated top/rear contacts in Si solar cells, Sol. Energy Mater. Sol. Cells **159**, 265 (2017)
84. B. Nemeth et al., Polycrystalline silicon passivated tunneling contacts for high efficiency silicon solar cells, J. Mater. Res. **31**, 671 (2016)
85. D. Yan et al., Phosphorus-diffused polysilicon contacts for solar cells, Sol. Energy Mater. Sol. Cell. **142**, 75 (2015)
86. R. Peibst et al., Working principle of carrier selective poly-Si/c-Si junctions: is tunnelling the whole story, Sol. Energy Mater. Sol. Cell. **158**, 60 (2016)
87. A. Richter, R. Muller, J. Benick et al., Design rules for high-efficiency both-sides-contacted silicon solar cells with balanced charge carrier transport and recombination losses, Nat. Energy **6**, 429 (2021)
88. JinkoSolar's High-efficiency N-Type Monocrystalline Silicon Solar Cell Sets Our New Record with Maximum Conversion Efficiency of 26.4%, Press Release by Jinko Solar (2022). https://www.jinkosolar.com/en/site/newsdetail/1827
89. S. Deng, Y. Cai, U. Roemer, F.-J. Ma, F. Rougieux, J. Huang, Y. Cheng, M.A. Green, N. Song, Mitigating parasitic absorption in Poly-Si contacts for TOPCon solar cells: A comprehensive review, Sol. Energy Mater. Sol. Cells **267**, 112704 (2024)
90. J. Stückelberger, G. Nogay, P. Wyss et al., Passivating electron contact based on highly crystalline nanostructured silicon oxide layers for silicon solar cells, Sol. Energy Mater. Sol. Cells **158**, 2 (2016)
91. G. Yang, P. Guo, P. Procel et al., Poly-crystalline silicon-oxide films as carrier-selective passivating contacts for c-Si solar cells, Appl. Phys. Lett. **112**, 193904 (2018)
92. J. Stückelberger, G. Nogay, P. Wyss et al., Passivating electron contact based on highly crystalline nanostructured silicon oxide layers for silicon solar cells, Sol. Energy Mater. Sol. Cells **158**, 2 (2016)
93. G. Yang, P. Guo, P. Procel et al., Poly-crystalline silicon-oxide films as carrier-selective passivating contacts for c-Si solar cells, Appl. Phys. Lett. **112**, 193904 (2018)
94. M. Singh, R. Santbergen, L. Mazzarella et al., Optical characterization of poly-SiOx and poly-SiCx carrier-selective passivating contacts, Sol. Energy Mater. Sol. Cells **210**, 110507 (2020)
95. M. Singh, R. Santbergen, I. Syifai et al., Comparing optical performance of a wide range of perovskite/silicon tandem architectures under real-world conditions, Nanophotonics **10**, 2043 (2021)
96. M. Singh, K. Datta, A. Amarnath et al., Crystalline silicon solar cells with thin poly-SiOx carrier-selective passivating contacts for perovskite/c-Si tandem applications, Prog. Photovolt. Res. Appl. **31**, 877 (2023)
97. A. Ingenito, G. Nogay, J. Stuckelberger et al., Phosphorous-doped silicon carbide as front-side full-area passivating contact for double-side contacted c-Si solar cells, IEEE J. Photovolt. **9**, 346 (2018)
98. G. Nogay, A. Ingenito, E. Rucavado et al., Crystalline silicon solar cells with coannealed electron- and hole-selective SiCx passivating contacts, IEEE J. Photovolt. **8**, 1478 (2018)
99. R. Santbergen, T. Meguro, T. Suezaki et al., GenPro4 optical model for solar cell simulation and its application to multijunction solar cells, IEEE J. Photovolt. **7**, 919 (2017)
100. A. Calcabrini, H. Ziar, O. Isabella et al., A simplified skyline-based method for estimating the annual solar energy potential in urban environments, Nat. Energy **4**, 206 (2019)
101. R. Santbergen, V.A. Muthukumar, R.M.E. Valckenborg, W.J.A. van de Wall, A.H.M. Smets, M. Zeman, Calculation of irradiance distribution on PV modules by combining sky and sensitivity maps, Sol. Energy **150**, 49 (2017)
102. P. Ricchiazzi, S. Yang, C. Gautier et al., SBDART: A research and teaching software tool for plane-parallel radiative transfer in the Earth's atmosphere, Bull. Am. Meteorol. Soc. **79**, 2101 (1998)
103. M. Zeman, O. Isabella, S. Solntsev, K. Jäger, Modelling of thin-film silicon solar cells, Sol. Energy Mater. Sol. Cells **119**, 94 (2013)

104. A. Ingenito, O. Isabella, S. Solntsev, M. Zeman, Accurate opto-electrical modeling of multi-crystalline silicon wafer-based solar cells, Sol. Energy Mater. Sol. Cells **123**, 17 (2014)
105. S. Mariotti, E. Köhnen, F. Scheler et al., Interface engineering for high-performance, triple-halide perovskite-silicon tandem solar cells, Science **381**, 63 (2023)
106. T. Jung, H. Song, H. Ahn, G. Kang, A mathematical model for cell-to-module conversion considering mismatching solar cells and the resistance of the interconnection ribbon, Sol. Energy **103**, 253 (2014)
107. A. Rehman, E.P. Van Kerschaver, E. Aydin et al., Electrode metallization for scaled perovskite/silicon tandem solar cells: challenges and opportunities, Prog. Photovolt. Res. Appl. **31**, 429 (2023)
108. R. Wittecka, H. Schulte-Huxela, H. Holst et al., Optimizing the solar cell front side metallization and the cell interconnection for high module power output, Energy Procedia **92**, 531 (2016)
109. M.Z. Jacobson, V. Jadhav, World estimates of PV optimal tilt angles and ratios of sunlight incident upon tilted and tracked PV panels relative to horizontal panels, Sol. Energy **169**, 55 (2018)
110. Y. Zhao, Hydrogenated nanocrystalline silicon-based layers for silicon heterojunction and perovskite/c-Si tandem solar cells, Ph.D. thesis, Delft University of Technology, 2023
111. C.U. Kim, J.C. Yu, E.D. Jung, I.Y. Choi, W. Park, H. Lee, I. Kim, D.K. Lee, K.K. Hong, M.H. Song, Optimization of device design for low cost and high efficiency planar monolithic perovskite/silicon tandem solar cells, Nano Energy **60**, 213 (2019)
112. A.D. Khan, F.E. Subhan, A.D. Khan, S.D. Khan, M.S. Ahmad, M.S. Rehan, M. Noman, Optimization of efficient monolithic perovskite/silicon tandem solar cell, Optik **208**, 164573 (2020)
113. M.T. Hörantner, H.J. Snaith, Predicting and optimising the energy yield of perovskite-on-silicon tandem solar cells under real world conditions, Energy Environ. Sci. **10**, 1983 (2017)
114. Y. Wu, A. Fell, K.J. Weber, A step-by-step optimization of the c-Si bottom cell in monolithic perovskite/c-Si tandem devices, Solar RRL **2**, 1800193 (2018)
115. G.J. Faturrochman, M.M. De Jong, R. Santbergen, W. Folkerts, M. Zeman, A.H.M. Smets, Maximizing annual yield of bifacial photovoltaic noise barriers, Solar Energy **162**, 300 (2018)
116. F.P. Gasparin, F.D. Kipper, F.S. Oliveira, A. Krenzinger, Assessment on the variation of temperature coefficients of photovoltaic modules with solar irradiance, Solar Energy **244**, 126 (2022)
117. M. Bastiani, A.J. Mirabelli, Yi. Hou et al., Efficient bifacial monolithic perovskite/silicon tandem solar cells via bandgap engineering, Nat. Energy **6**, 167 (2021)

Cite this article as: Manvika Singh, Jacopo Finazzo, Youri Blom, Mahesh Jayan, Carlos Ruiz Tobon, Arthur Weeber, Miroslav Zeman, Rudi Santbergen, Olindo Isabella, On the annual energy yield of perovskite/silicon tandem modules with different bottom cell technologies and optimized top cell properties for different locations, EPJ Photovoltaics **16**, 21 (2025), https://doi.org/10.1051/epjpv/2025009